Journal of Materials Chemistry C

ROYAL SOCIETY OF CHEMISTRY

PAPER

View Article Online
View Journal | View Issue

Cite this: J. Mater. Chem. C, 2026, 14, 7626

Photoswitchable carbosilane-based polycatenars forming nematic, tilted smectic, hexatic, and cubic liquid crystalline phases

Christian Anders, *[a] Yu Cao, [bc] Feng Liu, [bc] Srabony Sarkar, [a] Karsten Busse, [a] Carsten Tschierske *[a] and Mohamed Alaasar *[ad]

This study introduces a novel class of non-symmetric photoswitchable polycatenar liquid crystals (LCs) designed to investigate the influence of terminal chain architecture on mesophase behaviour and photo switching properties. These molecules feature a photoresponsive azobenzene core with distinct end groups: a linear alkoxy chain at one end and a branched carbosilane moiety, connected *via* an aliphatic spacer of varying length, at the other end. This non-symmetry promotes the formation of diverse LC phases, including nematic (N), smectic C (SmC), hexatic I (HexI), and a bicontinuous cubic phase with $Ia\bar{3}d$ space group ($Cub_{bi}/Ia\bar{3}d$). Small- and wide-angle X-ray scattering confirmed the presence of all observed LC phases. Comparison with the previously reported compounds having the flat taper-shaped 3,4,6-trialkoxyaryl substitution pattern instead of the tetrahedral carbosilane branching highlights the critical role of chain topology in controlling molecular self-assembly. UV-vis spectroscopy and polarized optical microscopy confirm efficient and reversible photoisomerization in solution and the bulk LC state, with light-triggered phase transitions (N ↔ Iso, SmC ↔ N). These results offer a promising pathway for designing advanced functional soft materials with integrated photoswitchable and structural complexity.

Received 3rd February 2026,
Accepted 25th February 2026

DOI: 10.1039/d6tc00353b

rsc.li/materials-c

1. Introduction

Liquid crystalline (LC) materials are widely used in different kinds of applications, such as optical displays,[1] organic electronics,[2] photovoltaics,[3] as templates for selective membranes,[4] biosensors,[5] and for nanoscale patterning at the sub-10 nm length scale used in nanolithography systems.[6] Essential for all these present and future technologies is the development of more efficient and faster stimuli-responding materials.[7,8]

LCs could be designed in different shapes, such as rod-like,[9] disc-like,[10,11] and bent-shaped structures.[12] Development of new functional materials is based on an ever-improving understanding of the structure–property relationships.[9] Depending on the molecular shape, molecular topology, and molecular amphiphilicity/polyphilicity, several types of LC phases could be expected.[13] While rod-like molecules with only one flexible chain at each end are mostly limited to the formation of nematic and smectic phases, multichain (so-called polycatenar) rod-like molecules were found to form many different LC phases, including smectic, columnar, and cubic phases, depending on the number of terminally attached flexible chains, ranging from three to six.[9,14–21] Recent studies have shown that polycatenar LCs having terminal chains non-symmetrically distributed between the two ends of the polyaromatic core can display spontaneous mirror-symmetry broken network phases,[22] such as chiral bicontinuous cubic phases with $I23$ space group ($Cub_{bi}/I23^{[*]}$),[23] tetragonal phases[24,25] and chiral isotropic liquids,[26] as well as an achiral double gyroid phase with $Ia\bar{3}d$ symmetry ($Cub_{bi}/Ia\bar{3}d$).[27] Such nonsymmetric polycatenars (see Scheme 1a) were designed with different shapes, including rod-like[28–36] and bent-shaped architectures.[8b,37,38]

Azobenzene-based symmetric[39,40] and non-symmetric polycatenars (see Scheme 1a),[35b,41] have attracted significant interest due to their unique combination of structural complexity and stimuli-responsive behaviour through reversible *trans–cis* photoisomerization. Their light-responsive behaviour is promising for photonic applications, including optically addressable switches, reconfigurable metamaterials, and adaptive optical elements,[12c,42] offering exciting possibilities for the

[a] Institute of Chemistry, Martin Luther University Halle-Wittenberg, 06120 Halle, Germany. E-mail: mohamed.alaasar@chemie.uni-halle.de
[b] Shaanxi International Research Center for Soft Matter, State Key Laboratory for Mechanical Behavior of Materials, Xi'an Jiaotong University, Xi'an 710049, P. R. China
[c] Institute of New Concept Sensors and Molecular Materials, Shaanxi Key Laboratory of New Concept Sensors and Molecular Materials, Xi'an Jiaotong University, Xi'an, 710049, P. R. China
[d] Department of Chemistry, Faculty of Science, Cairo University, 12613 Giza, Egypt. E-mail: malaasar@sci.cu.edu.eg

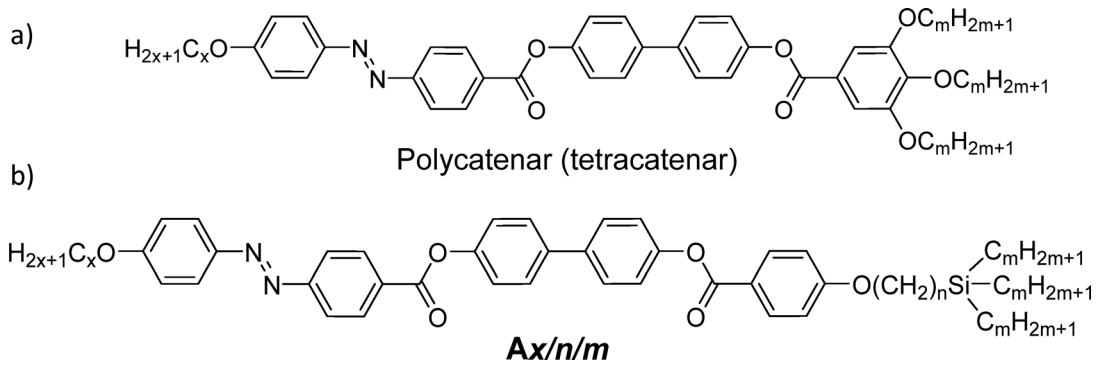

Scheme 1 Chemical structures of non-symmetric azobenzene-based multichain rod-like compounds: (a) non-symmetric tetracatenar with a 3,4,5-trialkoxy substitution pattern at one end[41] and (b) the carbosilanes **Ax/m/n** under discussion herein with a tetrahedral Si-based branching point in one end-chain.

development of advanced functional materials. Furthermore, their ability to display spontaneous mirror symmetry breaking in different phases (*e.g.*, $Cub_{bi}/I23^{[\star]}$ and $Iso_1^{[\star]}$, see Section 3.5)[35b,41] provides new avenues for exploring chirality transfer, chirality amplification[26] and circular polarized emission[43] in soft matter formed by achiral molecules. The phenomenon of emergent chiral structures from achiral molecules is especially prominent in systems featuring a 3,4,5-trialkoxy-substituted benzene at one end and a single chain at the other end of a polyaromatic backbone (Scheme 1a).[22,23,32,44] In these compounds, the junctions of the three peripheral chains are fixed in the plane of the benzene ring, which provides a flat taper shape (Scheme 1). In contrast, non-symmetric rod-like polycatenar LCs with three long chains attached *via* a tetrahedral branching point remain almost unexplored. Synthetically, the easiest option is to use silicon as a tetrahedral branching point. In this case, also the distance between the polyaromatic core and the branching point can be modified by using alkylene spacer units $(-CH_2-)_n$ having different lengths, *n*. In most cases only $-SiMe_3$ groups or oligo(carbosilane) chains connecting two or three linear oligomethylene brigded $-SiMe_2-$ units in linear alkyl chains were investigated,[45–47] while the bulkier $-(CH_2)_n-SiR_3$ groups with three longer residues R were only once used in non-symmetric polycatenar mesogens (Fig. S16a) and were shown to remove LC phases for R larger than the ethyl group.[48] For oligothiophene rods, bulky carbosilane chains at both ends were used to improve solubility and processability.[49] In our previous work, we attached such bulky carbosilanes side-on as lateral chains at polyaromatic oligo(*p*-phenylene ethynylene) cores to design X-shaped polyphilic LC molecules.[50] A key unresolved question in polycatenar self-assembly is whether decoupling the branching point from the aromatic core *via* an aliphatic spacer can provide independent control over both mesophase topology and structural stability, compared to the commoly used direct 3,4,5-substitution at the benzene ring (Scheme 1). Furthermore, it remains unclear whether such carbosilane-based polycatenars can maintain efficient and reversible photo switching while exhibiting complex LC phases.

Herein, we report on the design, synthesis, and investigation of a novel class of functional non-symmetric azobenzene-based polycatenars featuring a linear alkoxy chain at one end of the aromatic core and a highly branched carbosilane chain at the other end (compounds **Ax/n/m**, Scheme 1b). Their light-responsive behaviour is promising for photonic applications, offering exciting possibilities for the development of advanced functional materials. These examples should be regarded as prospective opportunities motivated by the unique combination of smectics/hexatic polymorphs, bicontinuous cubic networks, and photoswitchability, rather than as established device implementations, and the present work is focused on elucidating the underlying structure–property relationships.

2. Experimental

2.1. Synthesis

The synthesis of the azobenzene-based compounds **Ax/n/m** was performed as illustrated in Scheme 2. The azobenzene-containing acids **3** with different chain lengths, $x = 6$ and 10, were synthesized using previously reported protocols.[35b] The synthesis of the bromo-substituted carbosilanes **5** was performed following the procedures reported in ref. 50, while that of the biphenylol **7** was done by acylation using the benzoyl chloride derived from **6**. In the final step, the acids **3** were converted to their acid chlorides and used in an acylation reaction with the phenol **7** to obtain the target materials. The general synthetic procedures, purification methods, and analytical data of the synthesized intermediates and final compounds **Ax/n/m** are provided in Section S3 of the SI.

2.2. Characterization

All compounds were characterized by polarizing optical microscopy (POM), differential scanning calorimetry (DSC), and small-angle as well as wide-angle X-ray scattering (SAXS and WAXS), and with the equipment described in Section S1 of the SI.

3. Results and discussion

The transition temperatures, their corresponding enthalpies, and mesophase assignments for all compounds are summarized

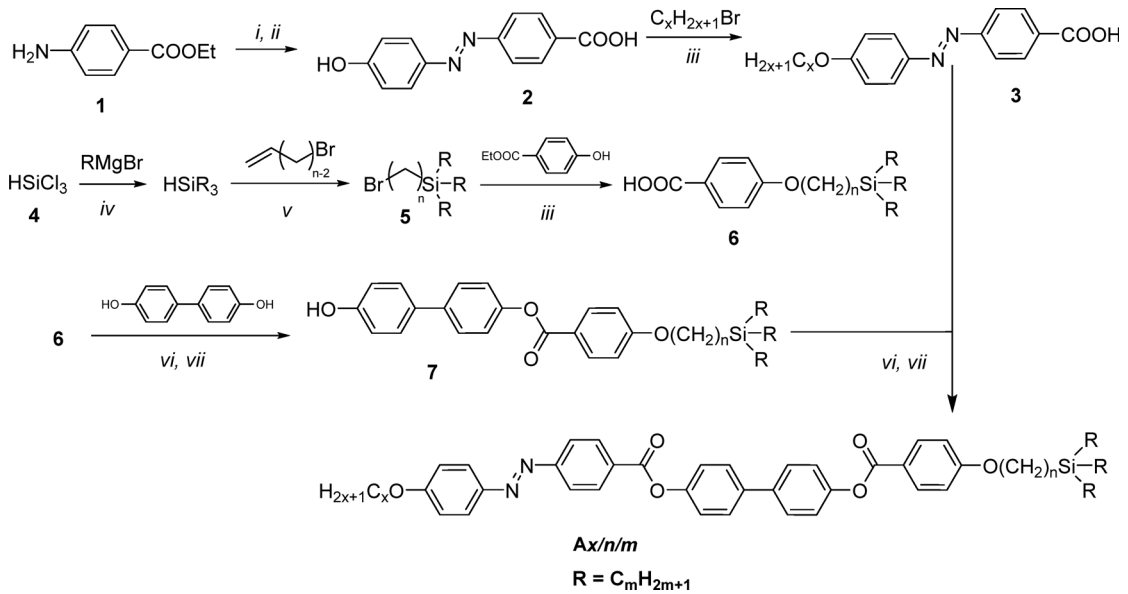

Scheme 2 Synthesis of the compounds **Ax/n/m**. Reagents and conditions: (i) $NaNO_2$, conc. HCl; (ii) Phenol, NaOH, Na_2CO_3; (iii) KOH, EtOH, 100 °C, 8 h; (iv) THF, LiCl, reflux, 1 h; (v) Karstedt-cat., CH_2Cl_2, RT, 1d, (vi) $SOCl_2$, DMF, reflux 1 h; (vii) CH_2Cl_2, Et_3N, pyridine, reflux, 6 h.

in Table 1 and illustrated graphically in Fig. 1. Notably, all mesophases were observed in heating and cooling cycles, thus representing enantiotropic LC phases with minor supercooling. Based on the number of carbon atoms (x) in the linear chain, the synthesized materials are divided into two groups. The first group is terminated with a short chain (x = 6), while the second group ends with a longer one (x = 10).

3.1. Short chain compounds A6/*n*/*m*

For the short-chain compounds with x = 6, depending on the spacer length (n) and the length of the chains (m) attached at the silicon atom, one or two different types of enantiotropic LC phases could be observed, as indicated by POM, DSC, and XRD investigations.

3.1.1. Compound A6/6/8 – SmC phase with continuous transition between the monolayer and the partial bilayer structure. For compound **A6/6/8** with x = n = 6 and m = 8, only one LC phase is found on heating and cooling under POM (see Fig. 2a for optical textures). This is also evident from the DSC investigations (Fig. 2b), where a single transition from the LC to the isotropic phase (Iso) is observed above the melting peak. Similarly, during the cooling cycle, only one transition

Table 1 Transition temperatures, enthalpies, and mesophases of compounds **Ax/n/m** ordered firstly according to growing alkyl chain length x, and secondly according to spacer length n[a]

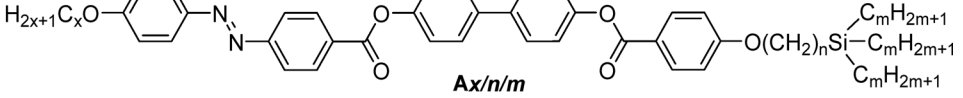

Comp.	x	n	m	T/°C [ΔH/kJ mol^{-1}]	L_C	V_C
A6/6/8	6	6	8	H: Cr 93 [14.8] SmC 252 [4.2] Iso C: Iso 249 [−3.7] SmC 91 [−11.3] Cr	20	36
A6/8/6	6	8	6	H: Cr 118 [8.3] Hex(I) 126 [0.4] SmC 286 [6.5] C: Iso 284 [−5.6] SmC 123 [−0.5] Hex(I) 115 [−7.4] Cr	20	32
A10/4/6	10	4	6	H: HexI 81 [2.3] SmC 236 [2.9] N_{CybC} 252 [0.4] Iso C: Iso 249 [−0.4] N_{CybC} 234 [−3.3] SmC 77 [−1.9] HexI	20	32
A10/6/6	10	6	6	H: Cr 83 [8.8] HexI 100 [0.5] SmC 257 [4.8] Iso C: Iso 254 [−4.5] SmC 97 [−1.1] HexI 77 [−8.8] Cr	22	34
A10/6/8	10	6	8	H: Cr 70 [7.4] HexI 87 [0.4] SmC 223 [1.5] $Cub_{bi}/Ia\bar{3}d$ 234 [1.8] Iso C: Iso 232 [−0.6] $Cub_{bi}/Ia\bar{3}d$ 220 [−1.9] SmC 85 [−0.8] HexI 66 [−7.0] Cr	24	40
A10/8/6	10	8	6	H: Cr 97 [7.0] HexI 109 [0.7] SmC 265 [5.3] Iso C: Iso 261 [−4.7] SmC 106 [−0.9] HexI 93 [−5.1] Cr	24	36

[a] Peak temperature as determined from 2nd heating (H) and 2nd cooling (C) DSC scans with a rate of 10 K min^{-1}; abbreviations: Cr = crystalline solid; Iso = isotropic liquid; N_{CybC} = cybotactic nematic phase composed of SmC clusters; SmC = synclinic tilted smectic phase, Hex(I), HexI = hexatic I phases (see Fig. 4e–g); $Cub_{bi}/Ia\bar{3}d$ = achiral bicontinuous cubic phase with $Ia\bar{3}d$ space group; L_C = total number of carbons in the total length of the alkyl chain = $x + n + m$; V_C = total number of carbons in the total volume of the alkyl chain = $x + n + 3m$ (Si and O were not counted); for DSCs, see Fig. 2b, 3a and 6d, and Fig. S1; for POM textures, see Fig. 2a, 3b and c, 5a–c and 6a–c and Fig. S2–S6; and For XRD, see Table 2.

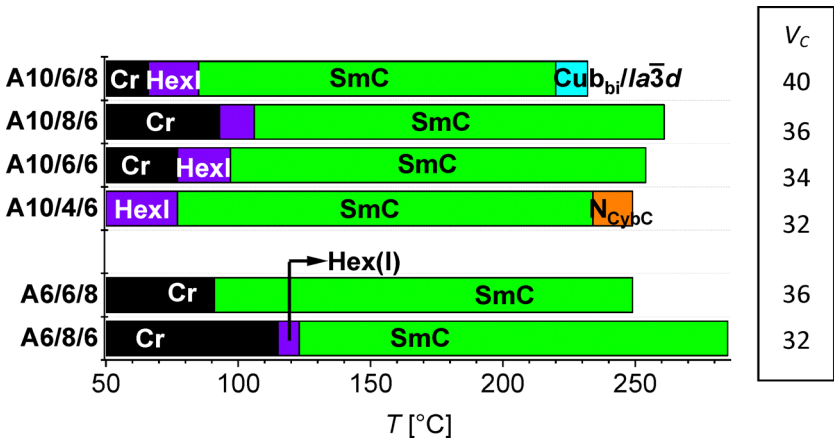

Fig. 1 Phase transitions of the investigated compounds **Ax/n/m** as a bar diagram ordered according to the *n*-alkyl chain length *x* and side chain volume (V_c), showing the mesophase type and the temperature range observed on cooling with a rate of 10 K min^{-1}; for numerical data and abbreviations, see Table 1.

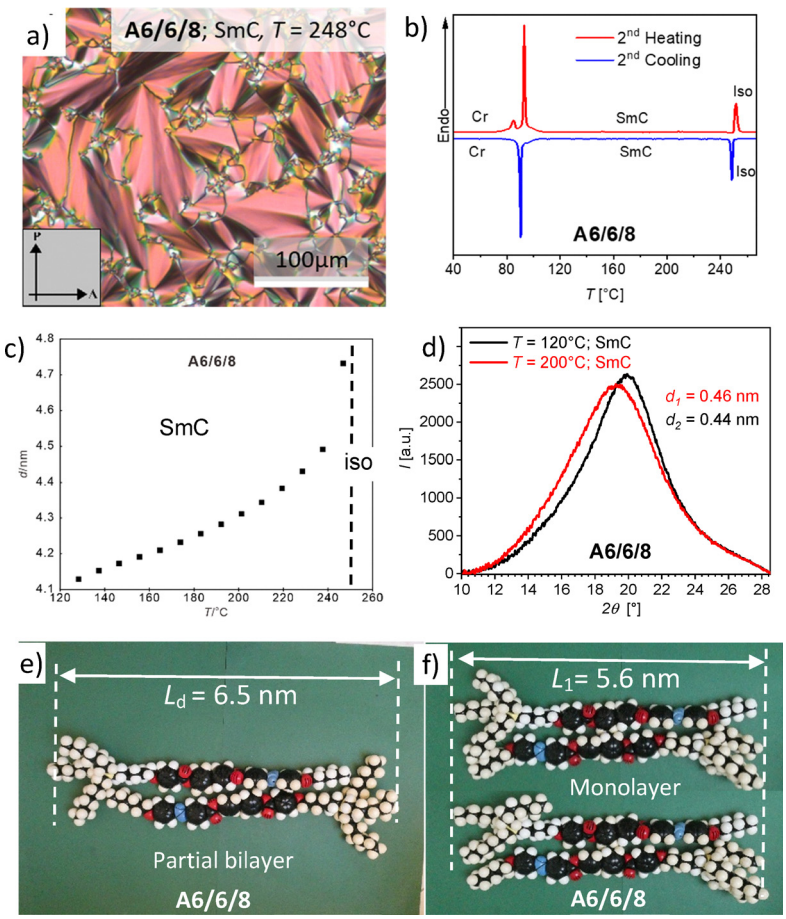

Fig. 2 Investigation of compound **A6/6/8**. (a) Optical texture observed under POM between crossed polarizers recorded in a non-coated 6 µm planar ITO cell at 248 °C (for additional textures, see Fig. S2, (b) DSC heating and cooling traces, recorded at 10 K min^{-1}; (c) *d*-value of the SAXS depending on temperature; (d) WAXS in the SmC phase at 120 and 200 °C, and (e and f) space filling CPK molecular models showing the lengths of pairs of antiparallel molecules in (e) the partial intercalated bilayer structure (L_d) and (f) the monolayer (fully intercalated) structure (L_1), corresponding to the molecular length (L_{mol}).

peak is recorded for the transition from the Iso state to the LC phase before the crystallization peak at ~91 °C. The LC phase range is relatively broad, with 159 K in heating and 158 K in cooling. Under POM in a planar cell, this LC phase is

characterized by a fan-shaped texture (Fig. 2a). The dark extinctions are inclined with respect to the polarizer and analyzer, as typical for a synclinic tilted SmC phase. The optical tilt, as determined by the inclination angle of the extinctions with respect to the polarizers, being a measure of the average tilt of the π-conjugated rod-like cores, is estimated to be around $ß_{opt} = 30 \pm 2°$, slightly decreasing upon cooling from 200 to 90 °C (Table S2).

In the X-ray scattering patterns, the WAXS is diffuse in the LC range with a maximum d = 0.46 nm at 200 °C and d = 0.44 nm at 120 °C, confirming LC phases and indicating a growing packing density on cooling (Fig. 2d). In aligned samples, the position of the WAXS is inclined with equator and meridian (Fig. S12c and d). From the position of the WAXS scattering maximum with respect to the direction of the layer reflections, an average tilt of $ß_{WAXS} = 38°$ with respect to the layer normal can be estimated at 200 °C and $ß_{WAXS} = \sim 35°$ at 120 °C (Table S2). This ''X-ray-tilt'' is a measure of the average of the combined tilt of cores and chains. That $ß_{WAXS}$ is larger than $ß_{opt}$ suggests that the alkyl chains contribute in this case a bit more to the average tilt than the rod-like cores. The temperature dependence of both, the optical tilt $ß_{opt}$, and the X-ray tilt $ß_{WAXS}$ in the SmC range is relatively weak, with $ß_{WAXS}$ decreasing only slightly from about 38° at high temperature to about 35° at the lower end of the SmC range, while $ß_{opt}$ remains in a similar range (see Table S2). This indicates that the pronounced change in layer spacing upon cooling is mainly associated with changes in the degree of intercalation rather than with a strong variation of the tilt angle.

The SAXS pattern of **A6/6/8** in the SmC phase at 200 °C shows a sharp layer reflection with a weak 2nd order reflection (Fig. S7a). The d-value is d = 4.74 nm at 247 °C and only d = 4.13 nm at 124 °C (Fig. 2c), being quite a bit shorter than the single molecular length of $L_{mol} = \sim 5.6$ nm (Fig. 2f and Table 2), in line with the tilted organization. The large change in the layer spacing at relatively small tilt angle variation suggests that the molecular packing changes with temperature. An antiparallel organization of the molecules allows a temperature-dependent change of the degree of intercalation. The shortest possible length of such a fully intercalated pair would correspond to the single molecular length, *i.e.*, $L_1 = L_{mol}$ = 5.6 nm (Fig. 2f). Assuming this mode of monolayer packing (SmC_1) and $ß_{opt} = 35°$, an effective molecular length L_{eff} = 5.04 nm is calculated according to $L_{eff} = d/\cos ß$ = 5.04 nm, being closer to L_{mol} = 5.6 nm. The ratio L_{eff}/L_{mol} = 0.9 can be attributed to orientational and conformational disorder of the molecules in the LC state.

The significantly larger d-value at higher temperature (d = 4.74 nm at 247 °C) at almost constant tilt (Table S2) cannot be attributed to a decreasing order parameter, because this would, in contrast, decrease the layer spacing. The only possibility is a reduction of the degree of intercalation between the molecules and a continuous transition to a partial intercalated bilayer structure (SmC_d).[51,52] Based on the maximum layer distance d = 4.74 nm and a tilt angle of $ß_{WAXS} = 38°$, the maximum effective molecular length of **A6/6/8** can be estimated according to $L_{eff} = d/\cos ß$ = 4.74 nm/cos 38° = 4.74/0.79 nm = 6.0 nm, exceeding the single molecular length L_{mol} = 5.6 nm (Table 2). Considering the correction factor of 0.9 for the contribution of conformational and orientational disorder, a value of L_{eff} = 6.7 nm is obtained. This length is close to the length of the partial intercalated antiparallel dimer shown in Fig. 2e (L_d = 6.5 nm) with the single hexyl chain of one molecule located in the space besides the C_6-spacers of the other. For convenience, the molecular pair lengths L_1 and L_d used in this analysis are summarized in Table 2. This partial intercalation allows the best segregation of alkyl chains from the rigid aromatic cores and a minimized steric crowding in the alkyl chain layers. In the SmC range at low temperature, the layer spacing is much smaller (d = 4.13 nm, see Fig. 2c). This requires that in the antiparallel pairs in this tilted smectic phase, the hexyl end-chain of one molecule is located beside the three octyl chains of the Si-branched end of the other, and the relatively short C_6 spacer is parallel to a part of the rod-like aromatic core of the adjacent molecule. This leads to an overcrowding in the alkyl chain layers (4 chains arranged side-by-side *vs.* only 2 cores side-by-side). The reason for this mode of packing in the SmC phase is unclear, but it might allow some backfolding of one of the chains at the tetrahedral Si branching point, enabling an improved overall packing (see Fig. 2f, bottom). With rising temperature, a layer expansion takes place by reducing the intercalation of branched and linear end-groups Fig. 2f → e).

Table 2 Effective molecular lengths, d-values and X-ray tilt angles of aligned samples in the SmC and HexI phases[a]

Comp.	d_{max} SmC (T/°C)	d_{min} SmC (T/°C)	d_{min} HexI (T/°C)	d_{max} HexI (T/°C)	$L_1 = L_{mol}$ [0.9 L_1] (nm)	L_d [0.9 L_d] (nm)	L_C	V_C	$ß_{WAXS}$ (SmC)/°	$ß_{WAXS}$ (HexI)/°
A6/6/8	4.74 (247)	4.13 (124)	—	—	5.6 [5.0]	6.5 [5.9]	20	36	35–38	—
A6/8/6	4.44 (255)	4.26 (140)	4.30 (123)	4.37 (115)	5.6 [5.0]	6.5 [5.9]	20	32	42	38
A10/4/6	3.95 (230)	3.75 (130)	4.21 (77)	4.44 (70)	5.5 [5.0]	6.5 [5.9]	20	32	37	40
A10/6/6	4.12 (242)	3.96 (135)	4.07 (97)	4.12 (80)	5.8 [5.2]	6.7 [6.0]	22	34	39	41
A10/6/8	4.33 (220)	4.18 (120)	4.24 (83)	4.30 (75)	6.1 [5.5]	7.2 [6.5]	24	40	43	44
A10/8/6	4.36 (265)	4.25 (160)	n.d.	n.d.	6.1 [5.5]	7.0 [6.3]	24	36	42	43

[a] Abbreviations: d_{min}, d_{max} = minimal and maximal experimentally measured d-values of the (10) small angle X-ray scattering (see Fig. 4a and b and Fig. S7–S13); L_1 = length of a molecular pair in a hypothetic single layer smectic phase with fully intercalated antiparallel organization (SmC_1, Fig. 2f) = L_{mol}; L_d = length of a molecular pair in a hypothetical partial bilayer smectic phase (SmC_d, Fig. 2e), determined with space filling CPK models, see Fig. 2e, f and 5f, g, and Fig. S14, the values in square brackets are adjusted to orientational and conformational disorder of the molecules, corresponding to 0.9 $L_{1/d}$. $ß_{WAXS}$ = tilt as determined from the position of the WAXS in 2D patterns (Fig. 5h and i and Fig. S12 and S13); for optical tilt ($ß_{opt}$), see Table S2.

This supports the segregation of aromatic cores and aliphatic units (end-groups and spacers) into separate layers, probably driven by the stronger rigid-flexible incompatibility[13a] caused by the growing alkyl chain disorder at higher temperature.

3.1.2. Compound A6/8/6 – transition from SmC to a tilted hexatic phase. Keeping L_C = 20 fixed and decreasing the total chain volume from V_c = 36 in **A6/6/8** to V_c = 32 in **A6/8/6** results in increasing transition temperatures, enlarging the LC phase range by ~10 K on heating or cooling and the induction of a short range (~8 K on heating and cooling) of an additional mesophase below SmC, indicated by a small peak in the DSC traces (ΔH = 0.4–0.5 kJ mol^{-1}) at 126 °C on heating and at 123 °C on cooling (Table 1 and Fig. 3a). As can be seen from Fig. 3b, the SmC phase of **A6/8/6** is characterized by a Schlieren texture in the homeotropic region and the typical fan-shaped texture with extinctions inclined with respect to the polarizer and analyzer in planar alignment. The optical and WAXS tilt angles in SmC, and the low temperature phase are around 40 ± 2° (Table 2 and Table S2).

With lowering temperature, the birefringence increases in the temperature range of the SmC phase in line with increasing orientational order parameter. In the SAXS pattern the first, second and 4th order layer reflections can be observed in the SmC range (Fig. 4a), and an additional 3rd order layer reflection becomes visible at the transition to the low temperature phase (Fig. 4b). The *d*-value of 4.44 nm in this SmC phase at 255 °C is a bit smaller than that found for **A6/6/8** around the same temperature and it decreases to 4.26 nm at 140 °C (Fig. 4d). This suggests that there is a similar change of the packing from a partial bilayer structure (SmC_d) at higher to a monolayer structure (SmC_1) at low temperature, but with a smaller change of the degree of intercalation. Remarkably, there is a minimum for the *d*-value around 140 °C (d = 4.26 nm), after which the *d*-value starts growing again, already before the transition to the low temperature phase (Fig. 4d).

At the phase transition to the low temperature phase at 123 °C, the width of the WAXS (full width at half maximum, FWHM) decreases from: Δq = 2.42 nm^{-1} at 200 °C to Δq = 1.35 nm^{-1} at 117 °C, and its shape changes from a Lorentzian towards lambda-like (Fig. 4c). This suggests a transition from a smectic to a hexatic mesophase (Hex). In the hexatic phases, the molecules assume a (pseudo)hexagonal packing in the layers, while between the layers there is long-range lattice orientational order, but no long-range positional correlation, assuming so-called "bond orientational order".[53] There are three types of tilted hexatic phases, which are HexF, HexL, and HexI,[53–56] differing in the orientation of the tilt direction with respect to the in-plane lattice (see Fig. 4e–g). In the WAXS pattern of an aligned sample of **A6/8/6** at 120 °C, there is a weak diffuse scattering on the equator parallel to the meridian, which might be a hint at the (002) scattering of the local pseudohexagonal (*c*-centered monoclinic) lattice of the HexI phase (Fig. S12b).[54]

There is a change of the schlieren texture at the SmC–Hex transition, assuming a more diffuse appearance, which is also in line with a HexI phase (Fig. 3b and c). In the case of a HexF phase, the WAXS would be broader, no scattering would be expected on the equator, and in the homeotropic schlieren texture, a transition to a mosaic-like appearance would be expected.[57] Based on these observations, HexI occurs more likely than HexF, though a HexL structure[55,56] cannot be completely excluded. Probably, there is only weak coupling between the layers, and therefore, we use Hex(I) in this case. In the temperature range of the proposed Hex(I) phase, the *d*-value rises from d = 4.27 to 4.37 nm, just before crystallization sets in, as shown in (Fig. 4d). Such layer expansion was also reported for other SmC–HexI transitions.[54] It can be explained, at least in part, by the chain stretching due to reduced conformational mobility and increased orientational order parameter in the denser packed Hex(I) phase (for more discussion, see Section 3.4). Notably, the tilt angles remain essentially

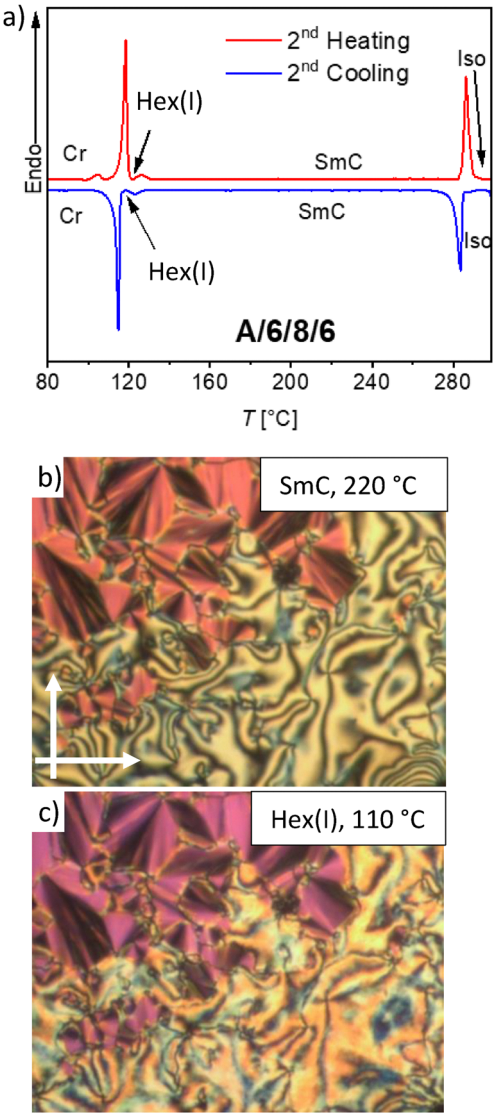

Fig. 3 Investigation of compound **A6/8/6**. (a) DSC heating and cooling traces, recorded at 10 K min^{-1}; (b and c) optical textures observed under POM between crossed polarizers for: fan-shaped and schlieren texture (b) of the SmC phase at 220 °C, and (c) of the Hex(I) phase at 110 °C recorded in non-treated glass plates.

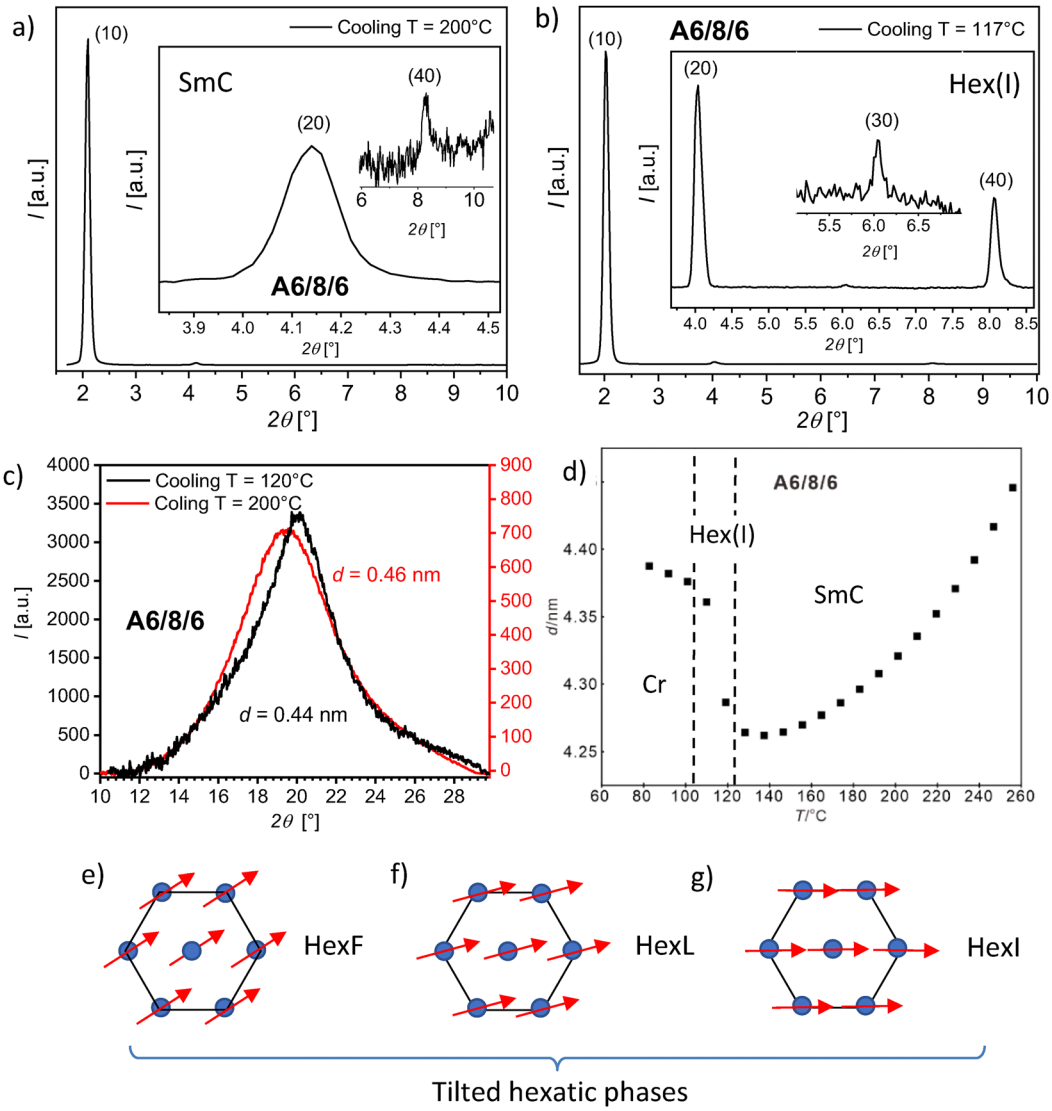

Fig. 4 X-ray investigation of compound **A6/8/6**. (a) SAXS pattern in the SmC phase at 200 °C and (b) in the Hex(I) phase at 117 °C, (c) WAXS at the indicated temperatures showing the shift to smaller distances and reduced line-width at the SmC–Hex(I) transition, (d) temperature dependence of the *d*-value on cooling and (e–g) the family of tilted hexatic phases with different tilt directions (red arrows) in view perpendicular to the layer plane.

constant across the SmC-to-Hex(I) transition, even though the layer spacing increases slightly in the Hex(I) phase (Fig. 4c and d and Table 2). This supports that the SmC-Hex(I) transition is driven primarily by changes in packing and bond-orientational order rather than by a significant change of tilt.

3.2. Long chain compounds A10/*n*/*m*

Using a longer terminal chain with $x = 10$ results in compounds **A10/*n*/*m***. All these compounds exhibit the SmC phase and a tilted hexatic low-temperature phase. However, in some cases, additional mesophases appear at higher temperatures (N and Cub) depending on the combination of *n* and *m* at the branched end (Table 1, Fig. 1).

3.2.1. Compound A10/4/6 – nematic – SmC – HexI transition. The first compound in this group with the smallest chain volume is **A10/4/6** with $V_c = x + n + 3m = 32$, which is equal to that of **A6/8/6**. The latter exhibited SmC and Hex(I) phases as discussed in the previous section, while **A10/4/6** exhibits an additional nematic phase between 249 and 234 °C (cooling data). Its formation with a characteristic schlieren texture in planar alignment was observed under POM (Fig. 5a). In the nematic phase, the relatively broad and intense small-angle scattering at $d = 4.16$ nm indicates a cybotactic nematic phase (Fig. S7c). X-ray scattering of aligned samples confirms a synclinic tilted organization with an average tilt of β_{WAXS} = 28° (Fig. S13a) in the cybotactic nematic phase composed of SmC clusters (N_{CybC}). The FWHM of the SAXS is about 0.66 nm^{-1}, indicating a longitudinal molecular coherence length of 9.5 nm, corresponding to about twice the *d*-value, *i.e.*, the clusters have a thickness of about two layers.

The change in the texture together with the XRD results confirms a phase sequence Iso-N_{CybC}-SmC-HexI upon cooling **A10/4/6** (Fig. 5a–c). The same phases are observed in reverse order upon heating. All phase transitions could also be

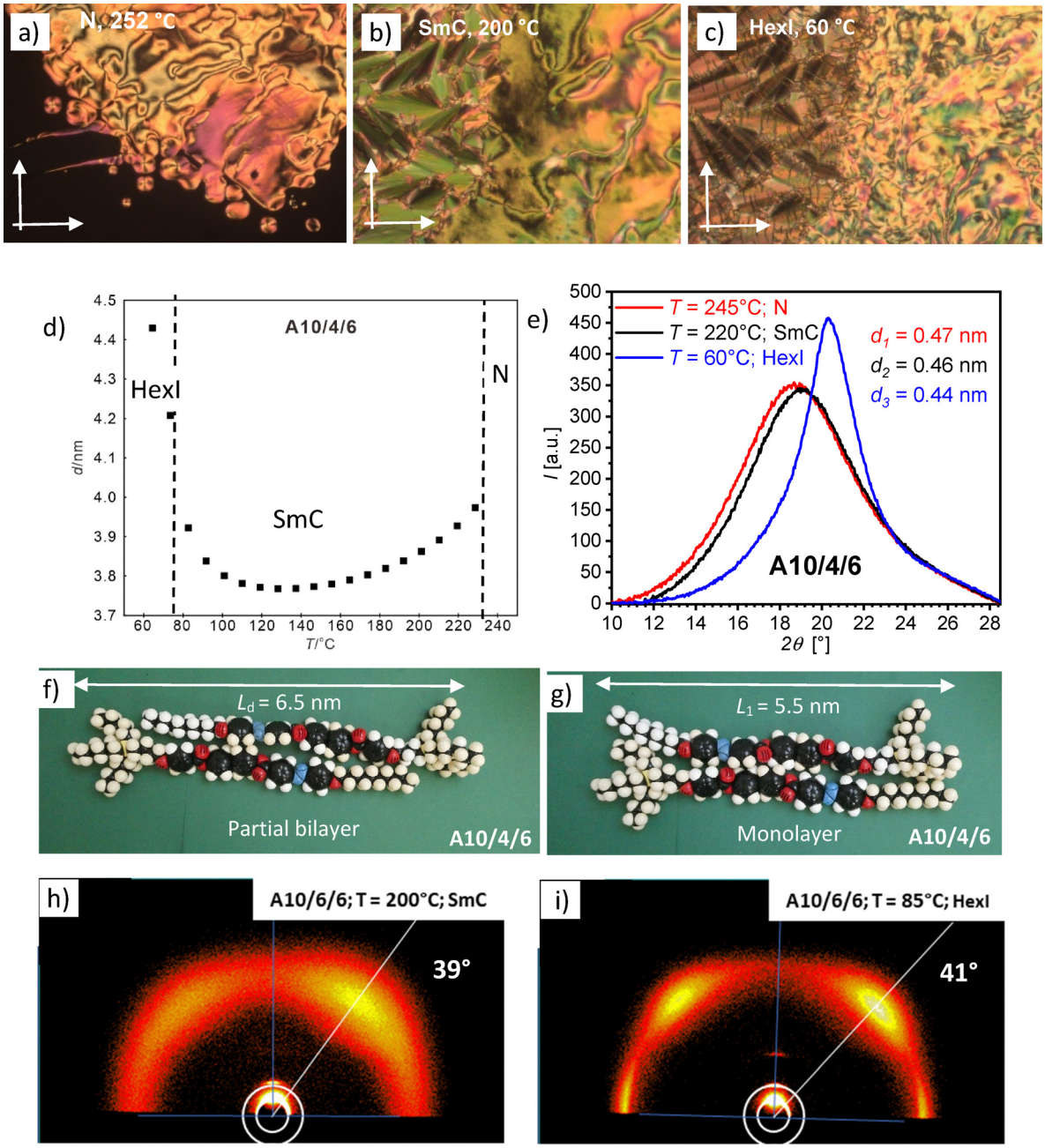

Fig. 5 (a–g) Data of compound **A10/4/6**. (a–c) Textures recorded on cooling by POM between non-treated glass plates recorded at the given temperatures (note that the change of birefringence of the fan texture takes place in the SmC range and not at the SmC–HexI transition, see Fig. S3); (d) *d*-value of the SAXS depending on temperature; (e) WAXS patterns and (f and g) space filling CPK molecular models showing pairs of antiparallel molecules of **A10/4/6**, in (f) with partial bilayer structure and in (g) in the monolayer structure; additional DSC scans are shown in Fig. S1a and additional XRD data in Fig. S7c–e and Fig. S13a–c. (h and j) Diffraction patterns of an aligned sample of compound **A10/6/6** in the SmC phase and (i) in the HexI phase (DSC in Fig. S1b, textures in Fig. S4, XRD in Fig. S8a, b and Fig. 10b).

recorded in heating and cooling cycles during DSC measurement (Fig. S1a). In this case, the lambda shape of the WAXS is well developed in the hexatic low-temperature phase (Fig. 5e), and in aligned samples, an additional WAXS on the equator is in line with an assignment of the hexatic phase to HexI (Fig. S13c). This scattering on the equator is found for all compounds with $x = 10$ (Fig. S13), and it is most clearly observed for **A10/6/6** (Fig. 5i). It appears that elongation of the linear end-chain supports the layer coupling, thus fixing a long-range orientational coupling of the hexagonal in-plane ordering between the layers. This also provides pronounced textural changes at the SmC–HexI transition as indicated by the transition to a broken fan texture and great changes in the areas with a schlieren texture (see Fig. 5b and c).

Moreover, the HexI phase of **A10/4/6** is a room temperature LC, which does not show any crystallization either on heating or cooling (Fig. S1a). This highlights the importance of the right selection of *x*, *n*, and *m* at both sides of the aromatic core to induce room temperature LC phases, which is an important characteristic from the application point of view. It also shows that not only the total chain volume but also the distribution and geometry of side chains – such as linearity *versus* branching and non-symmetry – play a critical role in determining the type and thermal range of mesophase formation.

Interestingly, **A10/4/6** shows the smallest *d*-values among the SmC phases of all investigated compounds, ranging between 3.75 and 3.95 nm (compared with d = 4.26–4.44 nm for **A6/8/6**, having the same total chain length L_C = 20, and total chain volume V_c = 32, see Fig. 5d and Table 2). The tilt angle is β_{WAXS} = 37° at 200 °C, only slightly smaller than that in the SmC phase of **A6/8/6** (β_{WAXS} = 42°), while there is almost no difference in the optical tilt (β_{opt} = 40/39°, Tables S2). The difference in the *d*-value could therefore not be traced back to different tilt angles. This would mean that for compounds with a long linear single chain (*x*) the fully intercalated monolayer structure (SmC_1) becomes more dominating, most probably, because it maximizes the core chain segregation (Fig. 5g). Note that this is just opposite to compounds **A6/*m*/*n*** where maximal core chain separation is found for the partial bilayer structure (SmC_d, see Fig. 2e). For **A10/4/6** the core chain segregation would be reduced by reducing the depth of intercalation upon transition to the partial bilayer phase at higher temperature (Fig. 5f). This explains that layer expansion becomes less favorable. Notably, in all cases with x = 10, there is an increase in the *d*-spacing upon approaching the HexI range. Thus, the minimum of *d*-spacing is achieved already in the SmC range, *ca.* 40–50 K, before transition to HexI (see Fig. 5d and Fig. S10 and Section 3.4).

The nematic phase was removed for the next compounds with $V_c \geq 34$ (Fig. 1). Thus, increasing the spacer length n to 6 results in the sequence of HexI-SmC-Iso for compound **A10/6/6** (see Fig. 5h and i, and Fig. S1b, S4, S9a, b, S10b and S11a). This indicates that changing the spacer length has a minor effect on the phase sequence because it only slightly changes the total chain volume (V_c). Elongation of the three end-chains at the silicon from m = 6 to 8 has a much larger steric effect.

3.2.2. Compound A10/6/8 – bicontinuous cubic phase. For compound **A10/6/8**, which has the largest side-chain volume among all synthesized compounds with V_c = 40, a sequence of two smectic phases and a three-dimensional bicontinuous cubic phase is observed (Fig. 1 and 6). All phase transitions could be detected during DSC investigations (Fig. 6d) and under POM (Fig. 6a–c). The high temperature LC phase is characterized by its isotropic appearance and high viscosity (Fig. 6a). The SAXS pattern with sharp reflections corresponding to a $1/d$ ratio of $\sqrt{6} : \sqrt{8} : \sqrt{14} : \sqrt{16} \ldots$ can be indexed to a cubic lattice with an $Ia\bar{3}d$ space group ($Cub_{bi}/Ia\bar{3}d$) and a_{cub} = 13.0 nm (Fig. 6e and Table S1). A broad diffuse scattering with a *d*-spacing of 0.47 nm confirms the absence of fixed molecular positions and hence supports the LC character of this cubic phase (Fig. S11b). The electron density map in Fig. 6f confirms a double gyroid bicontinuous cubic network

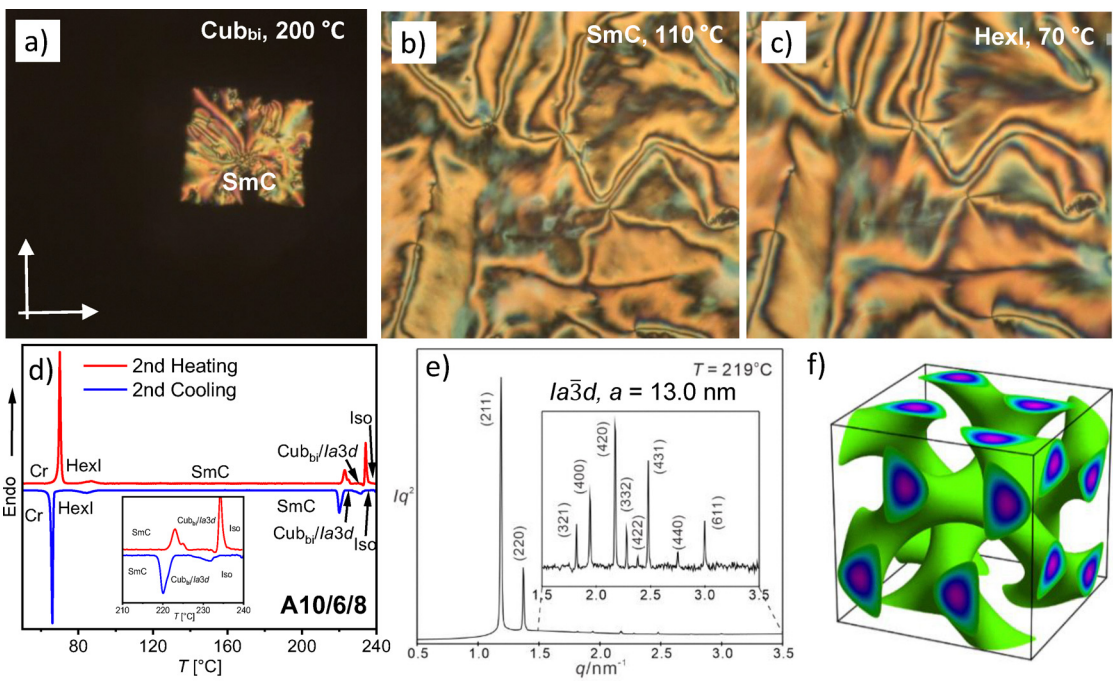

Fig. 6 Data of compound **A10/6/8**. (a–c) Textures recorded on cooling between crossed polarizers in thin films between ordinary glass plates: (a) Cub_{bi}/ phase at 200 °C; (b) SmC phase at 110 °C; (c) HexI phase at 70 °C (for XRD data, see Fig. S9, S10c and S11b); (d) DSC heating and cooling traces recorded at 10 K min^{-1}; (e) SAXS pattern in the cubic phase (for numerical data, see Table S1) and (f) electron density map reconstructed from this pattern; fan-like textures are shown in Fig. S5.

phase formed by two interwoven nets with trigonal three-way junctions formed by the polyaromatic rods in the continuum of the alkyl chains around the gyroid minimal surface, separating the two nets. There are two interwoven enantiomorphic networks (double gyroid), and within these networks, the polyaromatic cores are organized perpendicular to the struts in rafts of (on average) 4.7 side-by-side organized molecules, which are packed on top of each other with a uniform twist between them, with formation of a helical packing. The twist between the rafts is determined by the angle of 70.5° between the planes of the trigonal junctions and the number of rafts located between these junctions, the latter depending on the distance between the junctions. These parameters were calculated from the cubic lattice parameter as shown in Table S1. For the $Cub_{bi}/Ia\bar{3}d$ phase of **A10/6/8**, the twist between the rafts is Φ = 6.9°, and it is opposite in the two enantiomorphic nets, leading to an overall achiral *meso*-structure.[23,25,27]

On cooling the $Cub_{bi}/Ia\bar{3}d$ phase, a transition to the SmC phase (d = 4.17 nm, β_{WAXS} = 43°, Fig. 6a and Tables 1 and 2) takes place at ~220–200 °C, depending on cooling rate and other conditions, followed by a transition at ~85 °C to the HexI phase as indicated by textural changes (Fig. 6b → c) and the change of the WAXS scattering from a Lorentzian shape in Cub_{bi} and SmC, becoming narrower with lambda-shape and shifted to d = 0.44 nm at the transition to HexI (Fig. S11b).[53,54] The formation of the $Cub_{bi}/Ia\bar{3}d$ phase appears as a result of peripheral chain volume expansion at elevated temperature for this compound, with the largest V_C = 40, pushing the structure from a lamellar to a bicontinuous cubic phase.[22]

3.4. SmC–HexI transitions

Hexatic phases were previously mainly reported for rod-like mesogens with linear[57,58] and occasionally with branched end-chains,[59] for side-chain polymers,[60] and for a few Y-shaped tricatenar compounds (Fig. S16b).[36,44] All these cases obviously allow a sufficiently dense packing of the polyaromatic rods. However, the formation of hexatic phases for most of the compounds **Ax/*m*/*n*** with a highly branched carbosilane end-chain is surprising. It appears that the coupling of the lattice orientational order between the layers ("bond orientational order") is supported by elongation of the linear end chain (x = 6 → 10) combined with a relatively short branched end ($m + n \leq 12$). While increasing x strengthens the coupling, it appears that it is weakened by increasing n and especially m.

Often, the layer distance increases at the SmC–HexI transition due to the increased alkyl chain order, but it can also decrease if the tilt angle grows sufficiently strong. The $d = f(T)$ curves of compounds **Ax/*m*/*n*** (Fig. 4d and 5d, and Fig. S10) are very similar to those observed for recently reported Y-shaped tricatenars (Fig. S16b),[36] both assuming an antiparallel packing, and there is no significant change of the tilt at the SmC–HexI transition. In the SmC range, there is a decreasing layer spacing by a transition SmC_d → SmC_1 on cooling, competing with alkyl chain stretching at low temperature. This supports the organization in a partial bilayer structure where the alignment of the linear n-alkyl chain side-by-side with the π-conjugated rod (Fig. 5f) is more favorable at lower temperature than for the more flexible chains at higher temperature. Overall, the fully intercalated structure (monolayer, SmC_1, Fig. 7) has its highest stability at medium temperature, while at higher and lower temperatures the degree of intercalation decreases (→ partial bilayer structures SmC_d, $HexI_d$, Fig. 7). At lower temperature, it is the increased compatibility of the single rigid n-alkyl chains with the rigid rod units which expels the more disordered R_3Si groups into separate layers, while at high temperature it is the higher flexibility and disorder of the R_3Si groups which increases the segregation of these chains from the aromatic rods and linear n-alkyl chains (Fig. 7). The combination of chain stretching and adjustment of cross-sectional areas in the antiparallel pairs allows reaching a critical packing density and reduces intra- and intermolecular mobility, which enables layer coupling, though retaining a sufficient degree of disorder and packing frustration to inhibit crystallization. Thus, hexatic phase formation is not restricted to rod-like molecules with linear n-alkyl chains (strengthening the layer coupling), but it is obviously also supported by chain branching and polymerization, restricting denser packing and thus inhibiting (soft, like CrB, CrG, *etc.*, and solid) crystal formation.

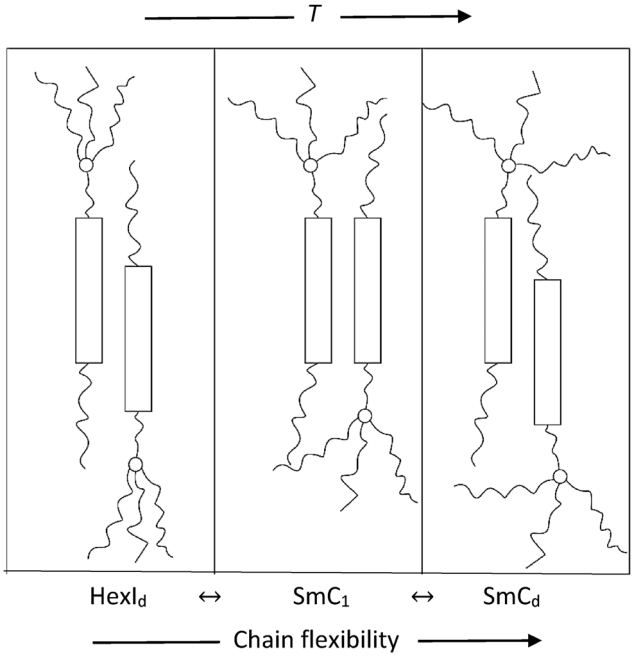

Fig. 7 Continuous change of the degree of intercalation of the molecules in the smectic and hexatic phases of compounds **Ax/*m*/*n*** shown for a pair of molecules.

For compounds **Ax/*n*/*m***, the transition SmC–HexI is associated with only a marginal change of the tilt angles (see Table 2 and Table S2), a significant increase of the layer spacing, and no recognizable change of birefringence (see, for example, Fig. S5b → c, S6b → c). The latter indicates that this transition is not associated with a significant increase of the orientational order parameter of the π-conjugated rods. Also, the packing

density (derived from the position of the WAXS maximum at d = 0.44 nm in all cases) achieved in the HexI-phase (for example **A10/4/6**, see Fig. 5e) is approximately the same as that found for the SmC phase of **A6/6/8** at the same temperature (Fig. 2d). Hence, it is concluded that the SmC–HexI transition, *i.e.* the onset of coupling of lattice orientational order is mainly due to the reduced molecular mobility at lower temperature and less to the direct effects of an increase in packing density or the orientational order parameter. This can be explained by the changing degree of rod-spacer intercalation (Fig. 7). As alkyl spacers become stretched at low temperature, the intercalation between rigid alkyl spacers and the aromatic core (in $HexI_d$) improves the packing, but simultaneously decreases the attractive arene–arene interactions, diminishing the energy gain due to increased order. Taken together, the data in Table 2 and Table S2 show that, for all investigated compounds, both $ß_{opt}$ and $ß_{WAXS}$ vary only modestly with temperature in the SmC range and exhibit no abrupt change at the SmC–HexI transition. Thus, the onset of hexatic order is best understood in terms of reduced molecular mobility and temperature-dependent intercalation, rather than a tilt-driven mechanism.

3.5. Comparison with related non-symmetric tetracatenars

To gain more insights about the effect of using a carbosilane unit as a branching center connected by an aliphatic spacer (n) to the aromatic core instead of connecting the multiple linear chains directly to the terminal benzene ring, the phase behavior of the new compounds **A10/6/8** and **A6/6/8** was compared with that of previously reported structurally related 3,4,5-trialkoxybenzoyl based polycatenars **B10/10** and **B6/10** (Fig. 8).[41] These compounds also have an azobenzene-based aromatic core with a comparable length (involving 5 benzenes and two COO units) and four flexible terminal chains, non-symmetrically distributed at both ends. However, while **B10/10** and **B6/10** feature a taper-like polycatenar structure with three linear alkoxy chains arranged in a plane at one end, the compounds in the present study have the 3 chains decoupled from the aromatic core and distributed in all three spatial directions by the tetrahedral carbosilane branching point. This difference leads to distinct volume distributions, conformational freedom, and degrees of lateral expansion of the chains.

These structural variations have a profound impact on the mesophase behavior. The total chain volume (V_c = 30 + x) of compounds **B6/10** and **B10/10** is 36 and 40 C-units, thus being comparable with those of **A10/6/8** and **A6/6/8**, respectively (Fig. 1). Firstly, the LC phase stability is significantly enhanced by the transition from compounds **B** to compounds **A** by almost 70–100 K, due to the decoupling of the branching point and core, thus allowing an easier parallel alignment of the polyaromatic cores, being not distorted by the lateral 3- and 5-substituents at the terminal benzene ring. Secondly, the SmC and HexI phases of series **A** are completely replaced by bicontinuous cubic phases in series **B**, indicating a stronger interfacial curvature by the trialkoxybenzoate units, providing a curvature directly at the aromatic–aliphatic interface. This stronger steric effect also leads to a stronger helical twist between the molecules along the networks in the cubic phases, giving rise to a transition from the achiral $Ia\bar{3}d$ phase for **A10/6/8** to a cubic network phase with $I23$ symmetry ($Cub_{bi}/I23^{[*]}$) for **B10/6** and **B10/10**,[22,23] capable of showing spontaneous mirror symmetry breaking in this cubic phase, as well as in the adjacent isotropic liquid phase assigned as $Iso_1^{[*]}$.[26] Moreover, in the series **B**, the $Cub_{bi}/I23^{[*]}$ phase is dominating over a broad temperature range, while in series **A**, the $Cub_{bi}/Ia\bar{3}d$ phase is observed for only one compound in a small temperature range. Despite the similar chain volume of the compounds **A** and **B**, the decoupling of the terminal chains from the aromatic backbone in the case of the compound **A** reduces the interfacial curvature and supports lamellar phases.

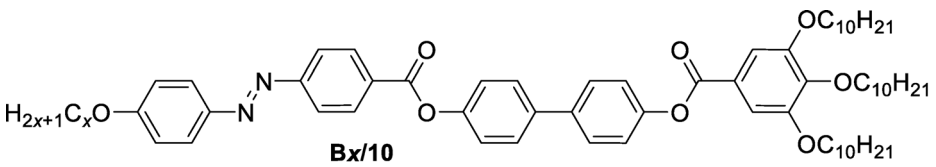

Bx/10

		V_C
B14/10 (x = 14)	**H:** Cr 51 X 77 $Cub_{bi}/I23^{[*]}$ 127 Tet_{bi} 147 $Cub_{bi}/Ia\bar{3}d$ 157 iso **C:** Iso 149 $Iso_1^{[*]}$ 144 $Cub_{bi}/Ia\bar{3}d$ 140 Tet_{bi} 30 Cr	44
B10/10 (x = 10)	**H:** Cr 76 $Cub_{bi}/I23^{[*]}$ 163 Iso **C:** Iso 160 $Iso_1^{[*]}$ 156 $Cub_{bi}/I23^{[*]}$ 20 Cr	40
B6/10 (x = 6)	**H:** Cr 88 $Cub_{bi}/I23^{[*]}$ 167 Iso **C:** Iso 167 $Iso_1^{[*]}$ 156 $Cub_{bi}/I23^{[*]}$ < 20 Cr	36

Fig. 8 Chemical structure of the non-symmetric tetracatenar compounds **Bx/10** with phase sequences and transition temperatures (°C) on heating (H) and cooling (C); abbreviations, $Cub_{bi}/I23^{[*]}$ = mirror-symmetry broken Cub_{bi} phase with an $I23$ space group; $Iso_1^{[*]}$ = mirror-symmetry broken isotropic liquid; Tet_{bi} = tetragonal network phase; and X = unknown mesophase, for other abbreviations, see Table 1; V_c = 30 + x (note that due to the absence of Si the chain volume of **Bx/10** is actually slightly (~1–2 C) smaller than that of **Ax/m/n**).[41]

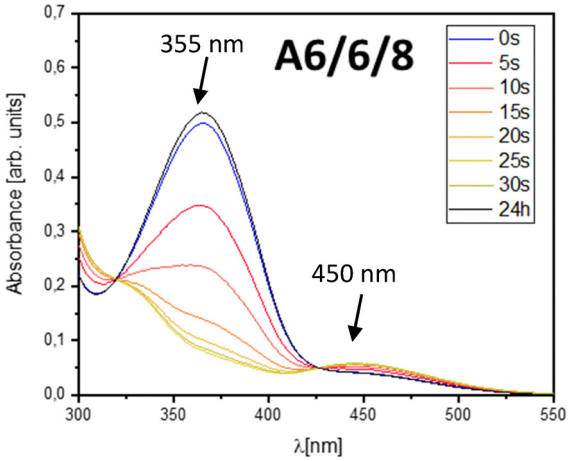

Fig. 9 UV-vis absorption spectra of compound **A6/6/8** in chloroform under 365 nm irradiation, showing reversible *trans–cis* photoisomerization. Time points from 0 s to 30 s and after 24 h of storage in the dark are shown.

A $Cub_{bi}/Ia\bar{3}d$ phase was also found in the series **B** for compound **B14/10** (Fig. 8) and higher homologues,[41] following the $Cub_{bi}/I23^{[\star]}$ phase at higher temperature, *i.e.*, with further alkyl chain expansion. Remarkably, despite the larger alkyl chain volume, the lattice parameter for **B14/10** is significantly smaller (a_{cub} = 11.1 nm)[41] compared to that of **A10/6/8** (a_{cub} = 13.0 nm). This means that for **A10/6/8** more rafts of molecules are required for a full twist by 70.5° between the trigonal junctions in the double gyroid network, *i.e.* the twist between the rafts of molecules in the $Ia\bar{3}d$ phase of **B14/10** (Φ = 8.1°) is larger than those in $I23^{[\star]}$ (Φ = 7.8°)[41] and the $Ia\bar{3}d$ phase (Φ = 6.9°) of **A10/6/8** (Table S1), in line with the phase sequence $Ia\bar{3}d$ (long pitch)-$I23^{[\star]}$–$Ia\bar{3}d$ (short pitch).[22,23,32] Moreover, the number of molecules in the cross section of the struts (twisted ribbons) between the nodes in the $Ia\bar{3}d$ phase of **A10/6/8**, *i.e.* the width of the rafts, is 4.7 molecules (Table S1), which are larger than the 3.2–3.5 molecules found in the cubic phases of **B14/10**.[41] This means that the spacer in series **A** leads to a smaller steric effect of the triply branched chain, compared to that of the 3,4,5-trialkoxy substituted terminus, which is also in line with the preferred appearance of smectic and hexatic phases.

These results indicate the importance of different parameters, which must be taken into consideration during the molecular design of functional soft materials. Reducing the spacer length *n* in compounds **A** is expected to couple the bulky carbosilane group closer to the aromatic core, which increases their steric effects and therefore should support the formation of cubic phases with curved interfaces and even might lead to new compounds with mirror symmetry broken cubic and isotropic liquid mesophases.

3.6. Photoswitching

The materials were designed to be photoswitchable by incorporating the azobenzene unit in their molecular architectures. To investigate the *trans–cis* photoisomerization under UV light, UV-vis absorption spectroscopy was performed in chloroform solution under 365 nm irradiation. The fresh sample of all materials exhibits a characteristic absorption band at ~355 nm corresponding to the π–π* transition and confirming the presence of the most stable *trans* isomer (Fig. S15). Upon light irradiation, all compounds showed a characteristic decrease in the π–π* transition band observed at ~355 nm and an increase in the n–π* band at ~450 nm, indicating conversion to the *cis*-isomer. As a representative example, compound **A6/6/8** (Fig. 9) exhibited a rapid decrease in the π–π* band within 15 seconds of irradiation, reaching a near-photo-stationary state by 30 seconds.

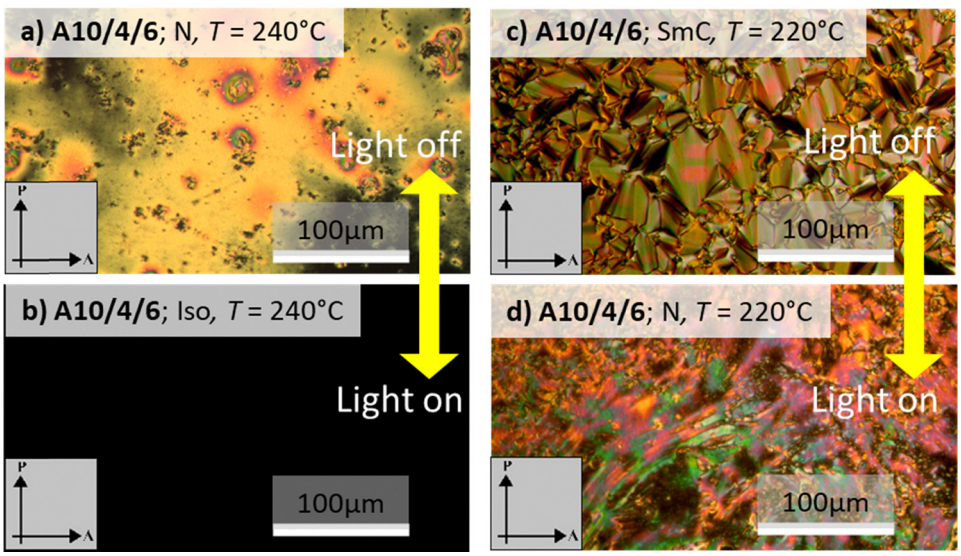

Fig. 10 Polarized optical micrographs of compound **A10/4/6**: (a) nematic texture before irradiation; (b) iso phase under 365 nm UV light; and (c) smectic C texture before irradiation. (d) N phase under 365 nm UV light.

The initial spectrum was fully recovered after 24 hours in the dark, demonstrating thermal back relaxation to the *trans*-isomer. Similar reversible photo-switching behavior was observed across the entire series (see Fig. S15), suggesting that side chain length and branching have a minimal influence on the photo-switching efficiency in solution.

In the LC phase, the effect of light-induced isomerization was evaluated using POM at elevated temperatures. Fig. 10 shows the photo response of compound **A10/4/6** as an example at 240 °C in the nematic (N) phase. Upon exposure to 365 nm UV light for less than 3 seconds, the birefringent nematic texture (Fig. 10a) converted to the optically isotropic texture of the isotropic liquid state (Fig. 10b), confirming a N-Iso phase transition under UV illumination. After switching off the light source, the nematic phase re-emerged within a few seconds, verifying an isothermal *cis-to-trans* back relaxation. Further investigation at 220 °C revealed a light-induced SmC-to-N phase transition for the same compound (**A10/4/6**). Upon UV irradiation, the SmC phase was destabilized, and the texture transformed into the nematic phase, indicating disruption of the smectic layers because of the bent molecules of the *trans*-isomer induced by light irradiation (Fig. 10c and d). A similar photo-induced HexI-SmC phase transition was investigated for **A10/4/6** by irradiation of the HexI at $T \sim 78$ °C on heating, where a rapid and reversible transition to the SmC phase was successfully achieved.

Altogether, these results demonstrate that these azobenzene-based polycatenars exhibit robust and reversible photo-switching ability in both solution and LC phases, offering potential for application as reconfigurable soft materials and in light-responsive LC devices.[61]

4. Conclusions

In summary, we have reported the design and synthesis of a new class of functional photo-switchable azobenzene-based polycatenars with carbosilane branching points. The materials have two different terminal groups, where one end bears a linear *n*-alkoxy chain, and the other has a bulky, branched three-armed carbosilane unit. This combination introduces a high degree of non-symmetry in volume distribution, which leads to a strict antiparallel organization of the molecules in strongly intercalated bilayers where polyaromatic cores and aliphatic chains are nano-segregated into separate layers. In order to avoid layer frustration due to the tendency of the bulky end-groups to induce an interfacial curvature, a significant tilt of the aromatic cores (β_{opt} = 30–43°, Table S2) is assumed, and the degree of intercalation is adjusted properly, leading to layer spacing adjustment.

The self-assembly of these materials was governed by the alkyl chain lengths (*x*, *n*, and *m*). This yielded two synclinic tilted lamellar phases: the SmC and the HexI phases. Notably, two distinct boundary behaviours emerged: compounds with the smallest chain volume formed a cybotactic nematic phase, while those with the largest chain volume stabilized a double gyroid network phase with cubic $Ia\bar{3}d$ symmetry. The formation of hexatic phases for most of these compounds with highly branched end chains is surprising and it is shown that the coupling of the lattice orientational order (''bond orientational order'') between the layers is supported by the long linear end chains (see Fig. 5g). It seems that reduced molecular mobility at lower temperature allows the orientational coupling of the developing in-plane hexagonal lattices, while packing density, orientational order and tilt angle appear to be not significantly changed at the SmC–HexI transition. It is proposed that the linear polyaromatic cores together with the linear alkyl chains allow a sufficiently dense and ordered packing to achieve lattice orientational layer coupling, while the branched end provides additional disorder and steric distortion, which prevents the denser packing in a solid crystalline lattice.

Beyond structural complexity, these materials also demonstrated reversible light-responsiveness. UV–Vis studies confirmed fast and reversible *trans–cis* photoisomerization in solution as well as in the LC state. UV irradiation triggered phase transitions such as N-to-Iso and SmC-to-N, with subsequent reformation of the original phases upon thermal relaxation. Therefore, this study establishes a new design framework for functional light-responsive materials based on non-symmetric polycatenars with branched carbosilane terminal groups. This work contributes to the broader goal of engineering responsive soft matter systems with complex and controllable self-assembly.

Conflicts of interest

There are no conflicts to declare.

Data availability

The data supporting this article have been included as part of the Supplementary Information (SI). Supplementary information is available. See DOI: https://doi.org/10.1039/d6tc00353b.

Acknowledgements

This work was supported by the Deutsche Forschungsgemeinschaft (DFG, AL2378/1-2, 424355983, 36494874 – GRK 2670) and the National Natural Science Foundation of China (12204369 and 22572151).

References

1 H. W. Chen, J. H. Lee, B. Y. Lin, S. Chen and S. T. Wu, *Light: Sci. Appl.*, 2018, **7**, 17168.
2 J. Uchida, B. Soberats, M. Gupta and T. Kato, *Adv. Mater.*, 2022, **34**, 2109063.
3 J. Wen, H. Lin, Y. Yu, M. Li, X. Du, J. Luo, G. Yang, C. Zheng and S. Tao, *ACS Appl. Energy Mater.*, 2022, **5**(10), 12809.

4 M. Henmi, K. Nakatsuji, T. Ichikawa, H. Tomioka, T. Sakamoto, M. Yoshio and T. Kato, *Adv. Mater.*, 2012, **24**, 2238.
5 K.-G. Noh and S.-Y. Park, *Adv. Funct. Mater.*, 2018, **28**, 1707562.
6 S.-M. Park, G. S. W. Craig, Y.-H. La, H. H. Solak and P. F. Nealey, *Macromolecules*, 2007, **40**, 5084.
7 F. Ercole, T. T. Davis and R. A. Evans, *Polym. Chem.*, 2010, **1**, 37.
8 (*a*) S. Bau, S. Li, Z. Tang, Y. Wan, G. Zhou, Z. Yang, D. Sun, D. Ye and L. Zhu, *J. Mater. Chem. C*, 2025, **13**, 9453; (*b*) Y. Cao, T. Nirgude, F. Dubois, D. P. Singh, F. Xi, F. Liu and M. Alaasar, *J. Mater. Chem. C*, 2026, **14**, 1799; (*c*) A. F. Darweesh, C. Anders and M. Alaasar, *RSC Adv.*, 2026, **16**, 1556.
9 ed J. W. Goodby, P. J. Collings, T. Kato, C. Tschierske, H. F. Gleeson, P. Raynes, *Handbook of Liquid Crystals*, 2nd edn, Wiley-VCH, Weinheim, Germany, 2014.
10 S. Chen, H. Taing, M. Ahmida, H. Y. He, A. Carr, H. M. Muchall and S. H. Eichhorn, *Soft Matter*, 2024, **20**, 7854.
11 T. Wöhrle, I. Wurzbach, J. Kirres, A. Kostidou, N. Kapernaum, J. Litterscheidt, J. C. Haenle, P. Staffeld, A. Baro, F. Giesselmann and S. Laschat, *Chem. Rev.*, 2016, **116**, 1139.
12 (*a*) R. A. Reddy and C. Tschierske, *J. Mater. Chem.*, 2006, **16**, 907; (*b*) H. Takezoe and A. Eremin, *Bent-shaped Liquid Crystals*, Taylor and Francis, Boca Raton, FL, 2017; (*c*) M. Alaasar, *Liq. Cryst.*, 2016, **43**, 2208.
13 (*a*) C. Tschierske, *Isr. J. Chem.*, 2012, **52**, 935; (*b*) C. Tschierske, *Angew. Chem., Int. Ed.*, 2013, **52**, 8828.
14 (*a*) J. Malthete, H. T. Nguyen and C. Destrade, *Liq. Cryst.*, 1993, **13**, 171; (*b*) H. T. Nguyen, C. Destrade and J. Malthete, *Adv. Mater.*, 1997, **9**, 375; (*c*) M. Ghatbia, A. Gharbi, H. T. Nguyen and J. Malthete, *Curr. Opin. Colloid Interface Sci.*, 2002, **7**, 312.
15 (*a*) D. W. Bruce, *Acc. Chem. Res.*, 2000, **33**, 831; (*b*) A. I. Smirnova, D. Fazio, E. F. Iglesias, C. G. Hall, D. Guillon, B. Donnio and D. W. Bruce, *Mol. Cryst. Liq. Cryst.*, 2003, **396**, 227.
16 T. Yasuda, H. Ooi, J. Morita, Y. Akama, K. Minoura, M. Funahashi, T. Shimomura and T. Kato, *Adv. Funct. Mater.*, 2009, **19**, 411.
17 M. Yoneya, *Chem. Rec.*, 2011, **11**, 66.
18 (*a*) A. K. Yadav, B. Pradhan, H. Ulla, S. Nath, J. De, S. K. Pal, M. N. Satyanarayan and A. S. Achalkumar, *J. Mater. Chem. C*, 2017, **5**, 9345; (*b*) S. Qu and M. Li, *Tetrahedron*, 2007, **63**, 12429; (*c*) M. L. Nguyen, J. Byun, S. Kim, J. W. Hyun, K. Hur, T. J. Shin and B.-K. Cho, *Angew. Chem., Int. Ed.*, 2019, **58**, 2749; (*d*) S. H. Eichhorn, A. J. Paraskos, K. Kishikawa and T. M. Swager, *J. Am. Chem. Soc.*, 2002, **124**, 12742.
19 (*a*) H. Cheng, Y. X. Li, X.-B. Zeng, H. Gao, X. Cheng and G. Ungar, *Chem. Commun.*, 2018, **54**, 156; (*b*) X. Du, T. Ma, Q. Chang, X. Liu and X. Cheng, *J. Mol. Liq.*, 2022, **351**, 118605.
20 Y.-X. Li, H.-F. Fao, R.-B. Zhang, K. Gabana, Q. Chang, Q. Chang, G. A. Gehring, X.-H. Cheng, X.-B. Zeng and G. Ungar, *Nat. Commun.*, 2022, **13**, 384.
21 (*a*) J. Kain, S. Diele, G. Pelzl, C. Liachka and W. Weissflog, *Liq. Cryst.*, 2000, **27**, 11; (*b*) C. Dessel, W. Weissflog and C. Tschierske, *Chem. Commun.*, 2015, **51**, 15850.
22 C. Dressel, T. Reppe, S. Poppe, M. Prehm, H. Lu, X. Zeng, G. Ungar and C. Tschierske, *Adv. Funct. Mater.*, 2020, **30**, 2004353.
23 (*a*) C. Dressel, F. Liu, M. Prehm, X. B. Zeng, G. Ungar and C. Tschierske, *Angew. Chem., Int. Ed.*, 2014, **53**, 13115; (*b*) X. Zeng and G. Ungar, *J. Mater. Chem. C*, 2020, **8**, 5389.
24 H. Lu, X. B. Zeng, G. Ungar, C. Dressel and C. Tschierske, *Angew. Chem., Int. Ed.*, 2018, **57**, 2835.
25 Y. Cao, M. Alaasar, L. Zhang, C. Zhu, C. Tschierske and F. Liu, *J. Am. Chem. Soc.*, 2022, **144**, 6936.
26 (*a*) C. Dressel, T. Reppe, M. Prehm, M. Brautzsch and C. Tschierske, *Nat. Chem.*, 2014, **6**, 971; (*b*) C. Tschierske and C. Dressel, *Symmetry*, 2020, **12**, 1098.
27 Y. Cao, M. Alaasar, A. Nallapaneni, M. Salamończyk, P. Marinko, E. Gorecka, C. Tschierske, F. Liu, N. Vaupotič and C. Zhu, *Phys. Rev. Lett.*, 2020, **125**, 027801.
28 E. Nishikawa, J. Yamamoto and H. Yokoyama, *J. Mater. Chem.*, 2003, **13**, 1887.
29 X. Zeng, L. Cseh, G. H. Mehl and G. Ungar, *J. Mater. Chem.*, 2008, **18**, 2953.
30 J. M. Wolska, J. Wilk, D. Poiecha, J. Mieczkowski and E. Gorecka, *Chem. – Eur. J.*, 2017, **23**, 6853.
31 (*a*) Y. Wang, S.-G. Yang, Y.-X. Li, Y. Cao, F. Liu, X.-B. Zeng, L. Cseh and G. Ungar, *Angew. Chem., Int. Ed.*, 2024, **63**, e202403156; (*b*) Y. N. Xue, X. B. Zeng, B.-W. Wu, Y.-X. Li, L. Cseh, S.-G. Yang, J. Liu, G. A. Gehring, F. Liu and G. Ungar, *Angew. Chem., Int. Ed.*, 2025, **64**, 3202505548.
32 (*a*) T. Reppe, C. Dressel, S. Poppe and C. Tschierske, *Chem. Commun.*, 2020, **56**, 711; (*b*) T. Reppe, S. Poppe, X. Cai, Y. Cao, F. Liu and C. Tschierske, *Chem. Sci.*, 2020, **11**, 5902; (*c*) T. Reppe, S. Poppe and C. Tschierske, *Chem. – Eur. J.*, 2020, **26**, 16066.
33 (*a*) M. Alaasar, A. F. Darweesh, X. Cai, Y. Cao, F. Liu and C. Tschierske, *Chem. – Eur. J.*, 2021, **27**, 14921; (*b*) M. Alaasar, A. F. Darweesh, C. Anders, K. Iakoubovskii and M. Yoshio, *Mater. Adv.*, 2024, **5**, 561; (*c*) M. Alaasar, Y. Cao, T. Neumann, T. Tan, F. Liu and M. Giese, *Mater. Adv.*, 2024, **5**, 8505; (*d*) M. Alaasar, X. Cai, F. Kraus, M. Giese, F. Liu and C. Tschierske, *J. Mol. Liq.*, 2022, **351**, 118597.
34 (*a*) O. Kwon, X. Cai, W. Qu, F. Liu, J. Szydlowska, E. Gorecka, M. J. Han, D. K. Yoon, S. Poppe and C. Tschierske, *Adv. Funct. Mater.*, 2021, **31**, 2102271; (*b*) O. Kwon, X. Cai, A. Saeed, F. Liu, S. Poppe and C. Tschierske, *Chem. Commun.*, 2021, **57**, 6491.
35 (*a*) M. Alaasar, S. Poppe, Q. Dong, F. Liu and C. Tschierske, *Angew. Chem., Int. Ed.*, 2017, **56**, 10801; (*b*) M. Alaasar, M. Prehm, Y. Cao, F. Liu and C. Tschierske, *Angew. Chem., Int. Ed.*, 2016, **128**, 320.
36 M. Alaasar, S. Poppe, Y. Cao, C. Chen, F. Liu, C. Zhu and C. Tschierske, *J. Mater. Chem. C*, 2020, **8**, 12902.
37 J. Matraszek, D. Pociecha, N. Vaupotič, M. Salamończyk, M. Vogrin and E. Gorecka, *Soft Matter*, 2020, **16**, 3882.

38 (*a*) M. Alaasar, X. Cai, Y. Cao and F. Liu, *New J. Chem.*, 2022, **46**, 15871; (*b*) M. Alaasar and S. Poppe, *J. Mol. Liq.*, 2022, **351**, 118613; M. Alaasar, A. F. Darweesh, Y. Cao, K. Iakoubovskii and M. Yoshio, *J. Mater. Chem. C*, 2024, **12**, 1523; (*c*) Y. Cao, Y. Zhao, T. Tan, F. Liu and M. Alaasar, *Chem. – Eur. J.*, 2025, **31**, e202403586; (*d*) Y. Cao, T. Nirgude, J. Jende, A. Jarosik, A. Eremin, F. Liu, M. Yoshio and M. Alaasar, *Adv. Mater. Interfaces*, 2026, DOI: 10.1002/admi.202501088.

39 N. G. Nagaveni, M. Gupta, A. Roy and V. Prasad, *J. Mater. Chem.*, 2010, **20**, 9089.

40 (*a*) X. Peng, H. Gao, Y. Xiao, H. Cheng, F. Huang and X. Cheng, *New J. Chem.*, 2017, **41**, 2004; (*b*) H. Chen, R. Zhang, H. Gao, H. Cheng, H. Fang and X. Cheng, *Dyes Pigm.*, 2018, **140**, 512.

41 M. Alaasar, Y. Cao, Y. Liu, F. Liu and C. Tschierske, *Chem. – Eur. J.*, 2022, **28**, e202201857.

42 (*a*) J. Hu, T. Song, M.-M. Yu and H. Yu, *Chem. Mater.*, 2023, **35**, 4612; (*b*) Z.-G. Zheng, Y.-Q. Lu and Q. Li, *Adv. Mater.*, 2020, **32**, 1905318; (*c*) H. Yu and T. Ikeda, *Adv. Mater.*, 2011, **23**, 2149; (*d*) H.-T. Yu, J.-W. Tang, Y.-Y. Feng and W. Feng, *Chin. J. Polym. Sci.*, 2019, **37**, 1183.

43 (*a*) Y. He, S. Li, J. Guo and Q. Li, *Aggregate*, 2021, **2**, e141; (*b*) Y. Imai, *Symmetry*, 2020, **12**, 1786; (*c*) F. Song, Y. Cheng, Q. Liu, Z. Qiu, J. W. Y. Lam, L. Lin, F. Yang and B. Z. Tang, *Mater. Chem. Front.*, 2019, **3**, 1768.

44 T. Reppe, C. Dressel, S. Poppe, A. Eremin and C. Tschierske, *Adv. Opt. Mater.*, 2020, 2001572.

45 (*a*) C. Keith, R. A. Reddy, H. Hahn, H. Lang and C. Tschierske, *Chem. Commun.*, 2004, 1898; (*b*) Y. Zang, U. Baumeister, C. Tschierske, M. J. O'Callaghan and C. Walker, *Chem. Mater.*, 2010, **22**, 2869; (*c*) E. Westphal, H. Gallardo, G. F. Caramori, N. Sebastian, M.-G. Tamba, A. Eremin, S. Kawauchi, M. Prehm and C. Tschierske, *Chem. Eur. J.*, 2016, **22**, 8181; (*d*) E. Westphal, H. Gallardo, N. Sebastian, A. Eremin, M. Prehm, M. Alaasar and C. Tschierske, *J. Mater. Chem. C*, 2019, **7**, 3064.

46 C. P. J. Schubert, C. Müller, A. Bogner, F. Giesselmann and R. P. Lemieux, *Soft Matter*, 2017, **13**, 3307.

47 (*a*) R. J. Mandle, E. J. Davis, C.-C. A. Voll, D. J. Lewis, S. J. Cowling and J. W. Goodby, *J. Mater. Chem. C*, 2015, **3**, 2380; (*b*) L. Fritsch, R. J. Mandle, S. J. Cowling and J. W. Goodby, *J. Mater. Chem. C*, 2021, **9**, 714.

48 J. Risse, A. Jakobi, W. Weissflog, D. Lose and S. Diele, *Proc. SPIE*, 1998, **3319**, 82, DOI: 10.1117/12.301257.

49 (*a*) A. Kreyes, A. Masoud, I. Lieberwirth, R. Mauer, F. Laquai, K. Landfester and U. Ziener, *Chem. Mater.*, 2010, **22**, 6453; (*b*) A. Kreyes, A. Mourran, Z. Hong, J. Wang, M. Möller, F. Gholamrezaie, W. S. C. Roelofs, D. M. de Leeuw and U. Ziener, *Chem. Mater.*, 2013, **25**, 2128; (*c*) W. H. de Jeu, K. Rahimi, U. Ziener, R. Vill, E. M. Herzig, P. Müller-Buschbaum, M. Möller and A. Mourran, *Langmuir*, 2016, **32**, 1533.

50 (*a*) C. Anders, M. Wagner, M. Alaasar, M.-V. Fischer, R. Waldecker, Y. Zhao, T. Tan, Y. Cao, F. Liu and C. Tschierske, *Chem. Commun.*, 2024, **60**, 1023; (*b*) C. Anders, T. Tan, V.-M. Fischer, R. Wang, M. Alaasar, R. Waldecker, Y. Cao, F. Liu and C. Tschierske, *Aggregate*, 2024, **5**, e728.

51 A. M. Levelut, R. J. Tarento, F. Hardouin, M. F. Achard and G. Sigaud, *Phys. Rev. A: At., Mol., Opt. Phys.*, 1981, **24**, 2180.

52 B. I. Ostrovskii, *Liq. Cryst.*, 1993, **14**, 131.

53 J. M. Seddon, in Structural Studies of Liquid crystals by X-ray diffraction, ed D. Demus, J. W. Goodby, G. W. Gray, H.-W. Spiess, V. Vill, *Handbook of Liquid Crystals*, Wiley-VCH, Weinheim, Germany, 1998, p. 635–679.

54 (*a*) P. A. C. Gane, A. J. Leadbetter and P. G. Wrighton, *Mol. Cryst. Liq. Cryst.*, 1981, **66**, 247; (*b*) P. A. C. Gane, A. J. Leadbetter, J. J. Benattar, F. Moussa and M. Lambert, *Phys. Rev. A: At., Mol., Opt. Phys.*, 1981, **24**, 2694; (*c*) J. J. Benattar, F. Moussa, M. Lambert and C. Germain, *J. Phys. Ltt.*, 1981, **42**, L-67.

55 G. S. Smith, E. B. Sirota, C. R. Safinya, R. J. Plano and N. A. Clark, *J. Chem. Phys.*, 1990, **92**, 4519.

56 C. Y. Chao, S. W. Hui, J. E. Maclennan, C. F. Chou and J. T. Ho, *Phys. Rev. Lett.*, 1997, **78**, 2581.

57 G. W. Gray and J. W. G. Goodby, *Smectic Liquid Crystals*, Leoard Hill, Glasgow, 1984.

58 (*a*) D. F. Ester and V. Williams, *Liq. Cryst.*, 2019, **46**, 76; (*b*) M. Piwowarczyk, A. Deptuch, A. Drzewicz, E. Juszynska-Galazka, Z. Galewski, S. Baran and M. Galazka, *J. Phys. Chem. B*, 2026, **130**, 909.

59 R. J. Mandle, N. Stock, S. J. Cowling, R. R. Parker, S. Hart, A. C. Whitwood and J. W. Goodby, *Liq. Cryst.*, 2019, **46**, 114.

60 (*a*) E. Martinelli, F. Paoli, B. Gallot and G. Galli, *J. Polym. Sci., Part A: Polym. Chem.*, 2010, **48**, 4128; (*b*) B. Gallot, G. Galli, A. Ceccanti and E. Chiellini, *Polymer*, 1999, **40**, 2561.

61 A. Goulet-Hanssens, F. Eisenreich and S. Hecht, *Adv. Mater.*, 2020, **32**, 1905966.

